

Multi-wavelength study of triggered star formation around 25 H II regions

Jin-Long Xu^{1,2}, Jun-Jie Wang^{1,2}, Chang-Chun Ning^{2,3} and Chuan-Peng Zhang^{1,2,4}

¹ National Astronomical Observatories, Chinese Academy of Sciences, Beijing 100012, China
xujl@bao.ac.cn

² NAOC-TU Joint Center for Astrophysics, Lhasa 850000, China

³ Tibet University, Lhasa, Tibet, 850000, China

⁴ University of the Chinese Academy of Sciences, Beijing, 100080, China

Abstract We have investigated 25 H II regions with bubble morphology in ¹³CO(1-0) and infrared data, to search the quantitative evidence for the triggering star formation by collect and collapse (CC) and radiatively driven implosion (RDI) models. These H II regions display the morphology of the complete or partial bubble at 8 μ m, which all are associated with the surrounding molecular clouds. We obtained that the electron temperature ranges from 5627 K to 6839 K in these H II regions, and the averaged electron temperature is 6083 K. The age of these H II regions is from 3.0×10^5 yr to 1.7×10^6 yr, and the mean age is 7.7×10^5 yr. Based on the morphology of the associated molecular clouds, we divided these H II regions into three groups, which may support CC and RDI models. We selected 23 young *IRAS* sources with the infrared luminosity of $>10^3 L_{\odot}$ in 19 H II regions. In addition, we identified some young stellar objects (including Class I sources), which are concentrated only in H II regions G29.007+0.076, G44.339-0.827, and G47.028+0.232. The polycyclic aromatic hydrocarbons (PAHs) emission of the three H II regions all show the cometary globule. Comparing the age of each H II region with the characteristic timescales for star formation, we suggest that the three H II regions can trigger the clustered star formation by RDI process. In addition, we for the first time detected seven molecular outflows in the five H II regions. These outflow sources may be triggered by the corresponding H II regions.

Key words: H II regions — ISM: bubbles —stars:formation—stars:protostars

1 INTRODUCTION

Isolated low-mass star formation has been well understood, the scenario of massive star formation and clustered star formation remain unclear. The feedback of massive star has significant impact on the surrounding environment, such as H II region, stellar winds, and supernova remnant (SNR)(Zinnecker & Yorke 2007, Dewangan et al. 2012). On the one hand, when these energetic products of massive star advance into the

form. On the other hand, when these energetic products of massive star collide with some pre-existing compact cloud cores, it will trigger the cloud cores to collapse. The triggered stars may form more quickly than quiescent isolated star formation. Moreover, since H II region, stellar winds, and SNR may impact on the large range of molecular clouds, then the clustered star formation may be triggered. Previous observations toward some SNRs (Junkes et al. 1992, Paron et al. 2009, Xu et al. 2011, Xu & Wang 2012) suggest that although some identified young stars are distributed around the SNRs, the obtained age of these SNRs is not enough large than time scales of young stars. What did trigger these young stars? SNRs may explode in the molecular shell produced by the H II region and/or stellar winds of their progenitor (Junkes et al. 1992, Paron et al. 2009, Su et al. 2009, Zhou et al. 2009), then the young stars found in the surrounding of SNRs may be triggered by the H II region and/or stellar winds.

Previous studies toward individual H II regions suggest that H II regions can trigger the young star formation (for example, Zavagno et al. 2010, Dewangan et al. 2012, Paron et al. 2011, Dirienzo et al. 2012). Two processes have been considered for the triggering of star formation at the edge of the H II regions, namely ‘collect and collapse (CC)’ (Dale et al. 2007) and ‘radiation driven implosion (RDI)’ (Sandford et al. 1982). In the CC process, a compressed layer of high-density neutral material forms between the ionization front and shock front preceding it in the neutral gas, and star formation occurs when this layer becomes gravitationally unstable, first proposed by Elmegreen & Lada (1997). Massive star formation may be triggered by CC process (Whitworth et al. 1994); In RDI process, the shocks drive into pre-existing density structures and compress them to form stars, which is characterized by the cometary globules or optically bright rims. Bright-rimmed clouds (BRCs) found in H II regions are potential sites of triggered star formation by RDI process. The RDI process may trigger the low-mass and intermediate-mass star formation (Reipurth 1983). Recently, observational searches for evidence of triggered star formation focused on Churchwell et al. (2006) bubbles. Churchwell et al. (2006) concluded that about 25% of the bubbles coincide with known radio H II regions, while Deharveng et al. (2010) suggested that about 86% of the bubbles contain ionized gas detected by the radio-continuum emission. Although nearly all GLIMPSE bubbles may be caused by H II regions, about half of all Galactic H II regions have a bubble morphology in the infrared band (Bania et al. 2010).

In this paper we will study 25 H II regions with bubble-like morphologies in a same way to analyze triggered star formation in H II regions. In Section 2, we summarize the selection of sample and young stars. In Section 3, we give the general results and discussion. In Section 4, we summarize our main conclusions.

2 DATA

2.1 Sample selection

The target sample was constructed by applying the following criteria: (1) The selected H II regions are in the GBT-Arecibo-GRS-NVSS-GLIMPSE surveys overlap regions. (2) The size of each selected H II region must be greater than the beam size of the surveys. (3) The selected H II regions have a bubble morphology at $8 \mu\text{m}$. From this criteria, we selected 25 H II regions as our sample, 16 of which are associated with

name, the Galactic longitude and latitude, the LSR velocity of H_{α} , and integrated flux density (S). The properties of these surveys are summarized below.

In the GBT survey (Anderson et al. 2011), 448 previously unknown Galactic H II regions were detected at X-band (9 GHz, 3 cm) in the Galactic zone $343^{\circ} \leq \ell \leq 67^{\circ}$ and $|b| \leq 1^{\circ}$. The FWHM beam size of the telescope is approximately $82''$ at this frequency. Additionally, in the Arecibo H II region surveys, Bania et al. (2012) reported the discovery of 37 previously unknown H II regions with the Arecibo telescope at X-band (9 GHz, 3 cm). The Galactic zone of survey is $31^{\circ} \leq \ell \leq 66^{\circ}$ with $|b| \leq 1^{\circ}$. Its beam is nearly three times smaller than that of the GBT.

To trace the ionized gas and investigate the molecular gas distribution of the surrounding H II regions, we used the NVSS and BU-FCRAO GRS surveys. NVSS is a 1.4 GHz continuum survey covering the entire sky north of -40° declination (Condon et al. 1998) with a noise of about 0.45 mJy/beam and the resolution of $45''$. While the GRS is a new survey of Galactic $^{13}\text{CO}(1-0)$ emission (Jackson et al. 2006). The survey covers a longitude range of $\ell = 18^{\circ} - 55.7^{\circ}$ and a latitude range of $|b| \leq 1^{\circ}$, with a angular resolution of $46''$. The survey's velocity coverage is -5 to 135 km s^{-1} for Galactic longitudes $\ell \leq 40^{\circ}$ and -5 to 85 km s^{-1} for Galactic longitudes $\ell > 40^{\circ}$. At the velocity resolution of 0.21 km s^{-1} , the typical rms sensitivity is 0.13 K .

GLIMPSE survey is used to identify the young stars along H II regions, which observed the Galactic plane ($65^{\circ} < |l| < 10^{\circ}$ for $|b| < 1^{\circ}$) with the four mid-IR bands (3.6, 4.5, 5.8, and $8.0 \mu\text{m}$) of the Infrared Array Camera (IRAC) (Fazio et al. 2004) on the Spitzer Space Telescope. The resolution is from $1.5''$ ($3.6 \mu\text{m}$) to $1.9''$ ($8.0 \mu\text{m}$).

3 RESULTS AND DISCUSSION

3.1 H II regions

3.1.1 The morphology of H II regions

Figure 1 (Right panels) shows the 1.4 GHz continuum emission contours (blue) superimposed on Spitzer-IRAC $8 \mu\text{m}$ image of each H II region (color scale). The $8 \mu\text{m}$ IRAC band contains emission from polycyclic aromatic hydrocarbons (PAHs). PAHs are believed to be destroyed in the ionized gas, but thought to be excited at the interface of H II region and molecular cloud by the radiation leaking from the H II region. Hence, the triggered formation of young stars are easily found in the molecular clouds adjacent to $8 \mu\text{m}$ emission. In Figure 1 (Right panels), the $8 \mu\text{m}$ emission display the morphology of the complete and partial bubble. The 1.4 GHz continuum emission reveals the presence of ionized gas in each H II region. From Figure 1 (Right panels), we can see that the $8 \mu\text{m}$ bubble of these H II regions are filled with the 1.4 GHz continuum emission, except for G19.813+0.010 and 50.039-0.274. Hence, PAH emission may be excited by the radiation leaking from these H II regions. In G41.928+0.029 region, there may be another H II region located at the northwest, which is surrounding by the shell-like molecular gas. Through the morphology at

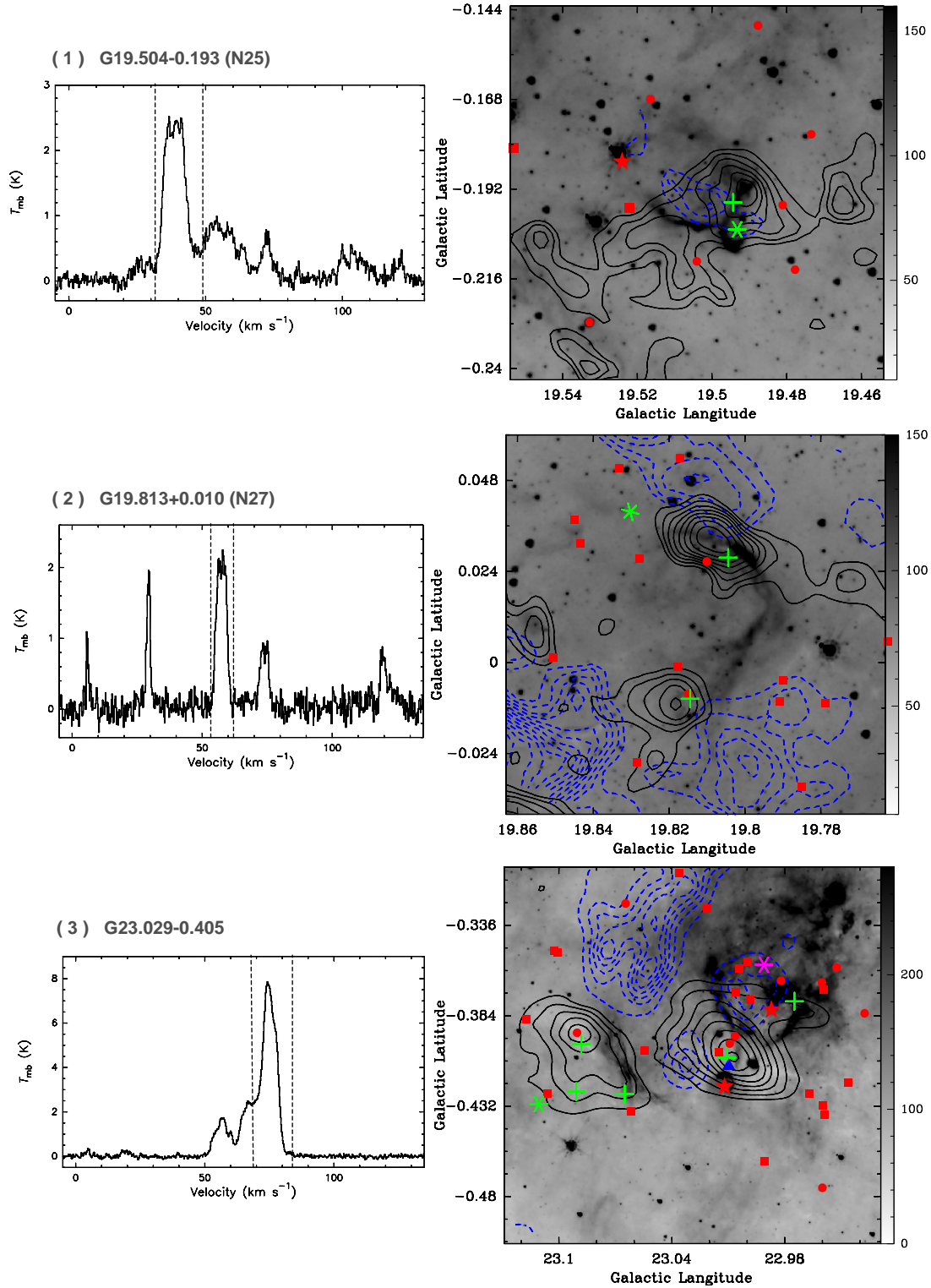
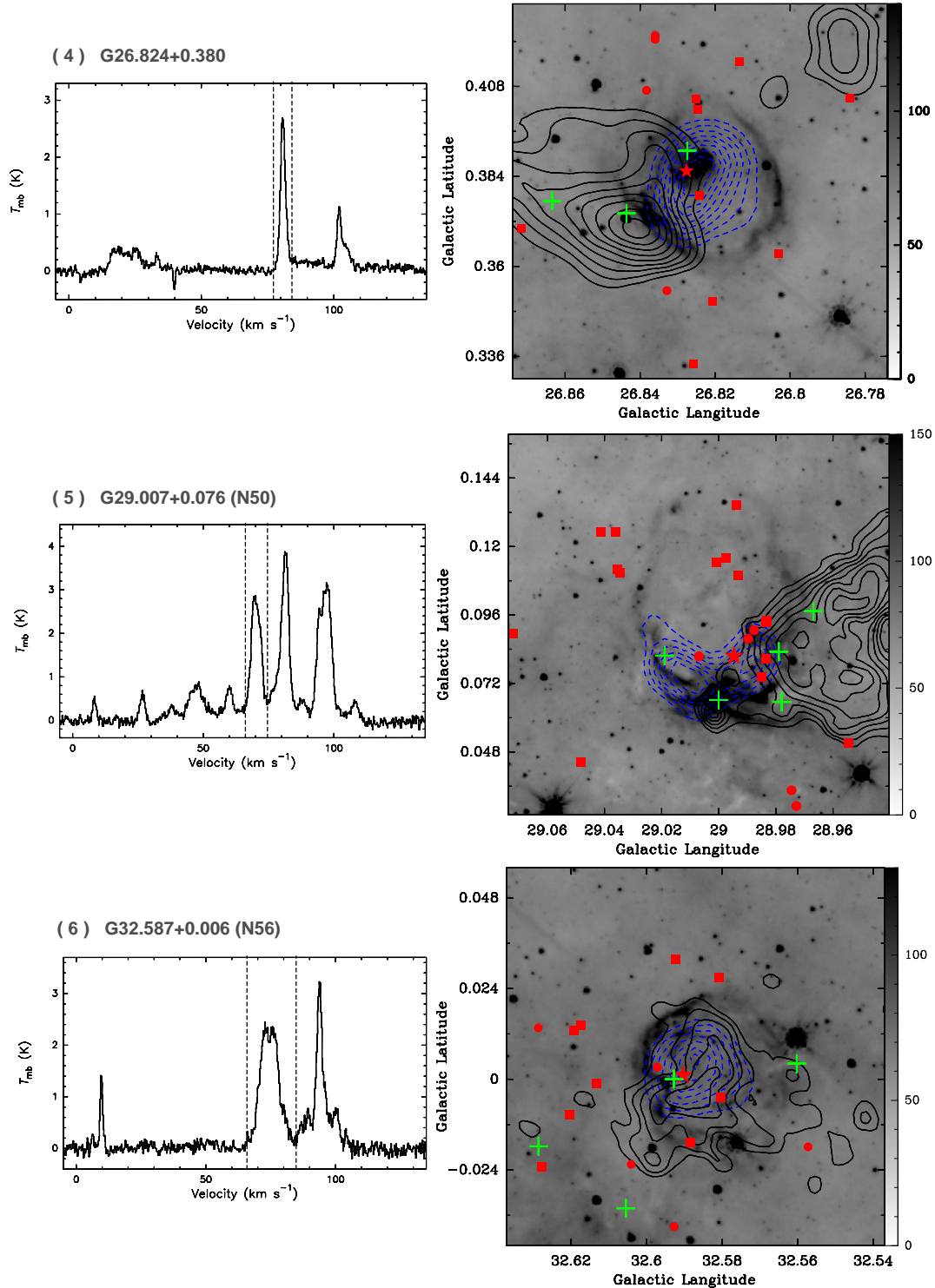
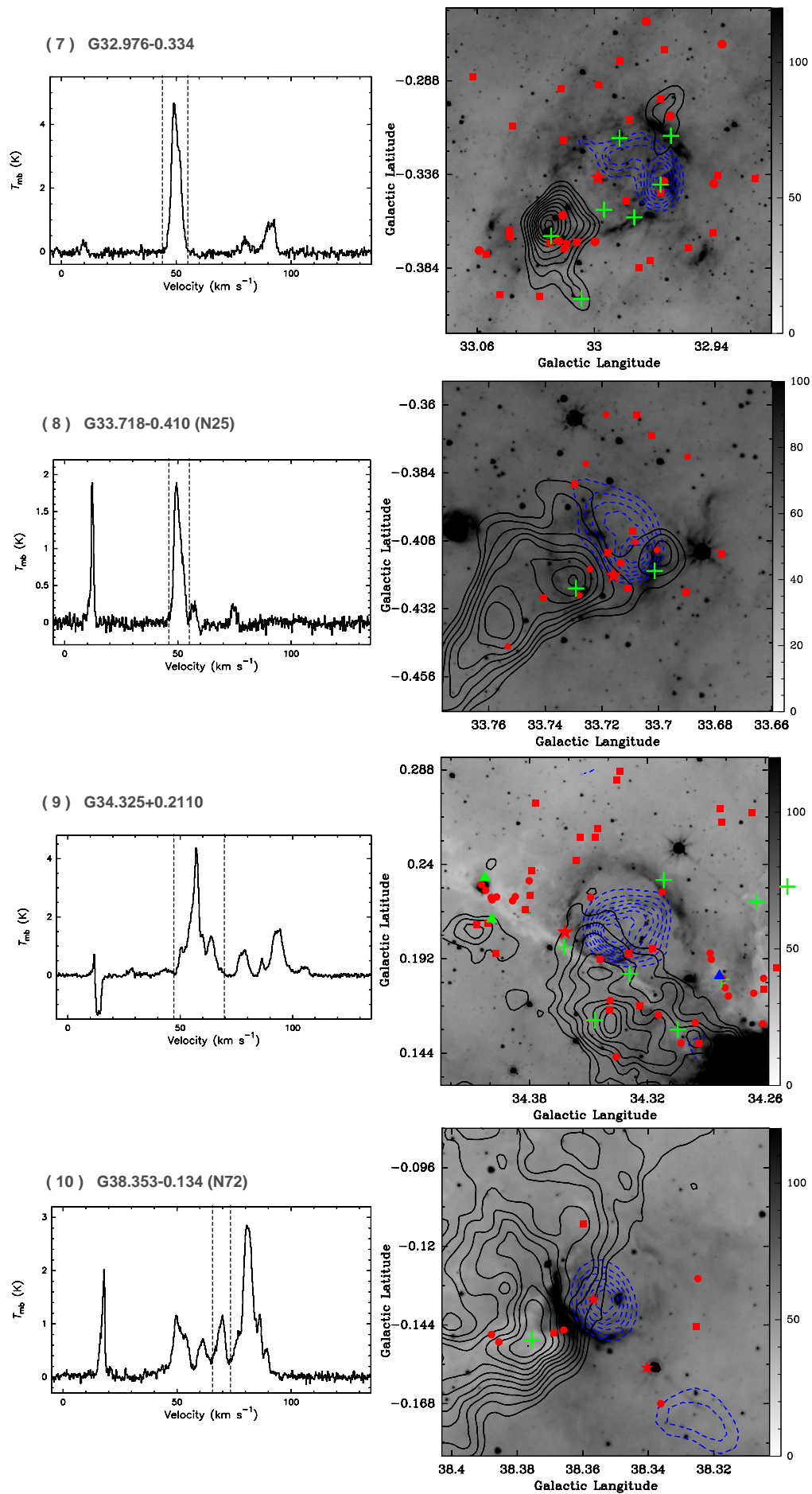
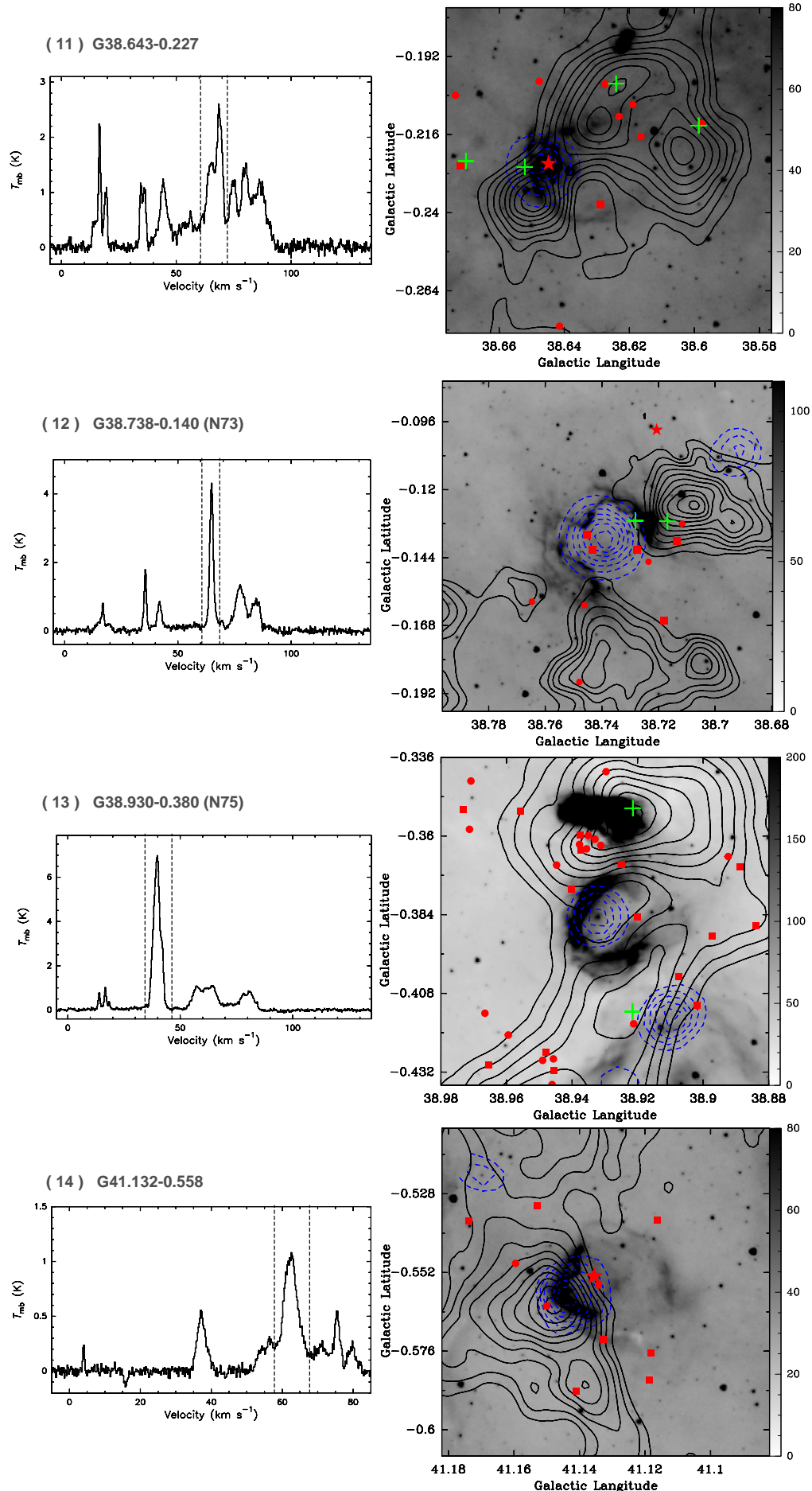


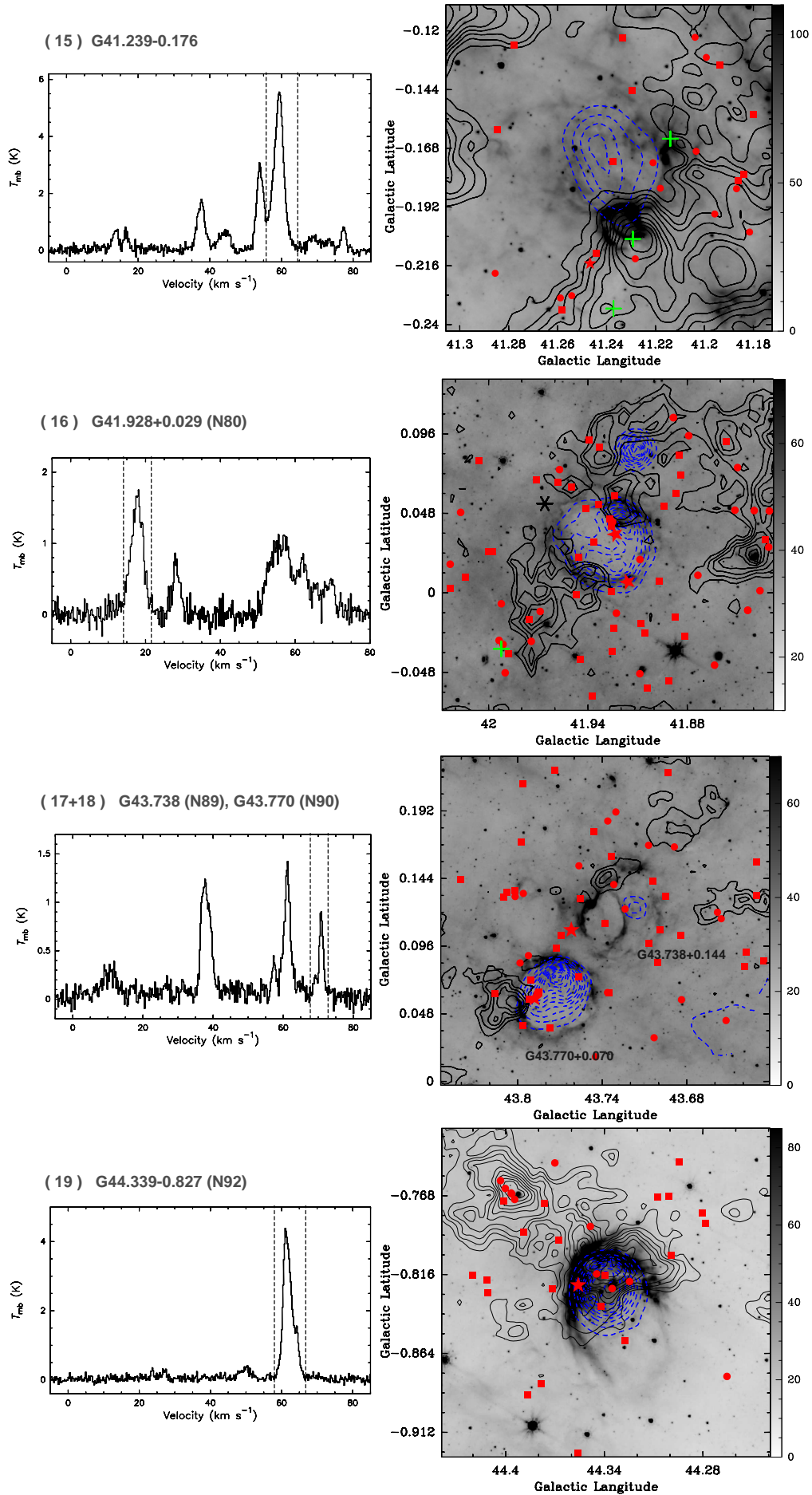
Fig. 1 Left panels: ^{13}CO J=1-0 spectral profile averaged over the molecular clouds. Two black dashed lines and red solid line mark the integrated velocity ranges and tangent point velocity, respectively. Right panels: ^{13}CO J=1-0 integrated intensity (black contours) and 1.4 GHz continuum emission (blue dashed contours) maps overlaid on the mid-infrared $8\ \mu\text{m}$ emission map (grey scale). The blue contour levels begin at the peak flux of 20% and increase in steps of the peak flux of 10%. Class I sources are labeled as the red dots, and Class II sources as the red filled square. The red stars represent IRAS sources. The green pluses and “*” indicate the millimeter

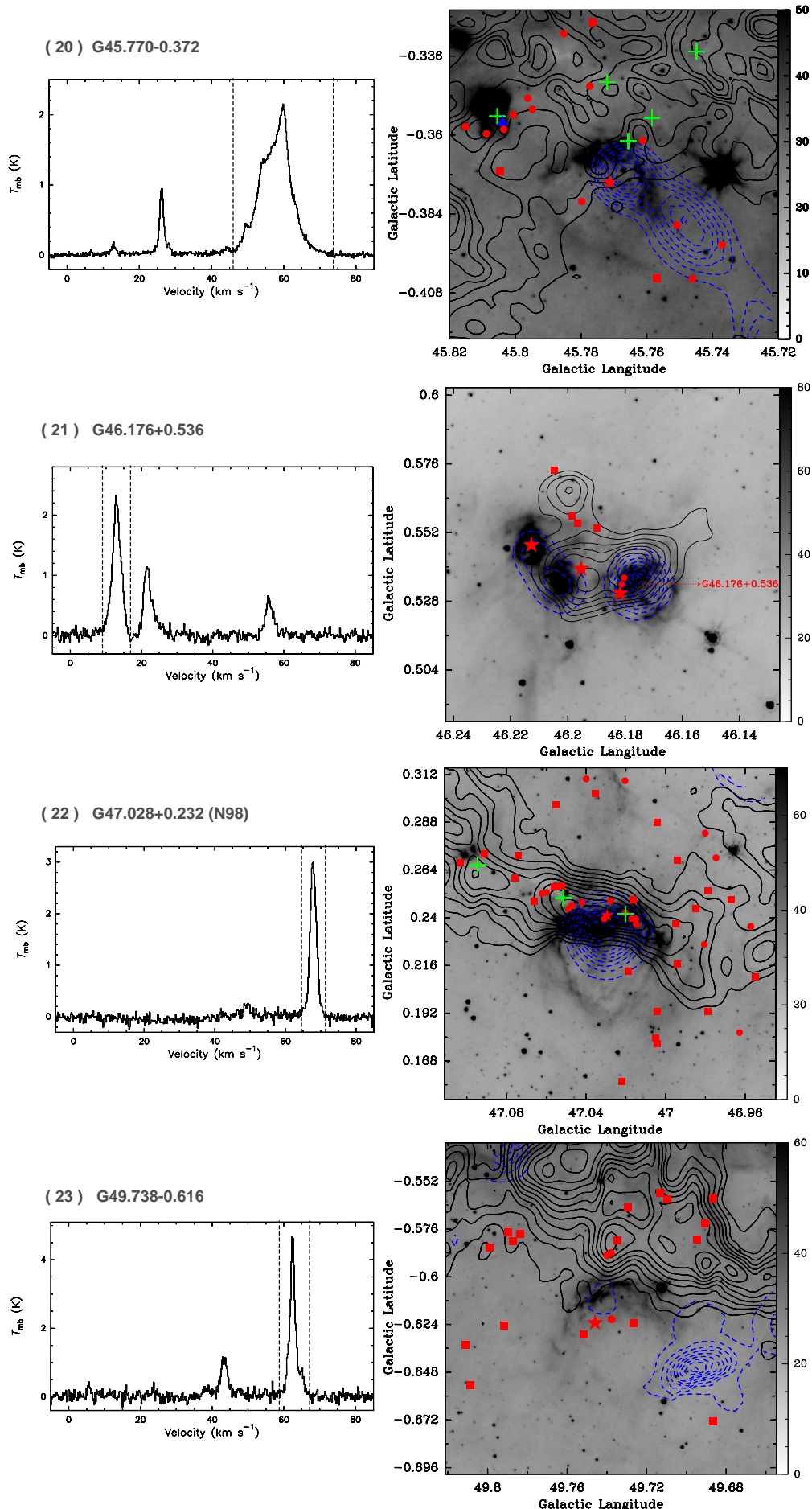


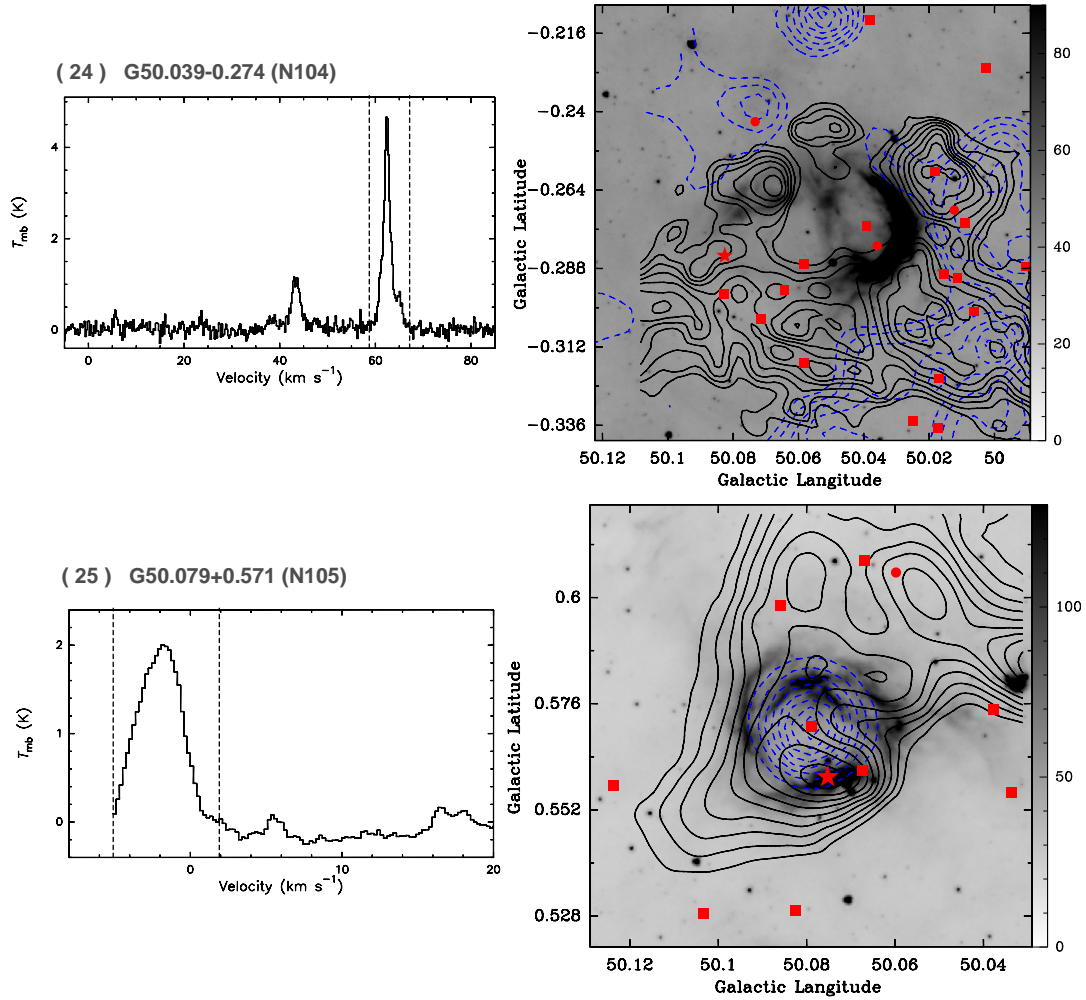
Continue: (4) 2.0, 2.4, 2.7, 3.1, 3.5, 3.8, 4.2, 4.5, 4.9 km s^{-1} . (5) 3.5, 4.0, 4.7, 5.4, 6.0, 6.7, 7.4, 8.0 km s^{-1} . (6) 5.2, 6.3, 7.3, 8.3, 9.4, 10.4, 12.5, 13.6, 14.6 km s^{-1} . (7) 5.2, 6.3, 7.3, 8.3, 9.4, 11.5, 12.5, 13.6, 14.6 km s^{-1} . (8) 2.5, 2.8, 3.1, 3.5, 3.8, 4.2, 4.5, 4.8 km s^{-1} . (9) 3.7, 4.3, 4.8, 5.4, 6.0, 6.5, 7.1, 7.7 km s^{-1} . (10) 5.9, 6.5, 7.1, 7.7, 8.3, 8.9, 9.5, 10.1, 10.7, 11.3, 11.8 km s^{-1} . (11) 5.3, 6.1, 6.9, 7.7, 8.5, 9.3, 10.2, 11.0 km s^{-1} . (12) 2.7, 3.3, 3.8, 4.3, 4.9, 5.4, 6.0, 6.5, 7.0, 7.6 km s^{-1} . (13) 7.6, 9.1, 10.7, 12.2, 13.7, 15.2, 16.7, 18.3, 19.8, 21.3 km s^{-1} . (14) 2.7, 3.2, 3.8, 4.3, 4.9, 5.4, 5.9, 6.5, 7.0, 7.5 km s^{-1} . (15) 4.2, 5.2, 6.2, 7.2, 8.2, 9.2, 10.2, 11.2 km s^{-1} . (16) 2.3, 3.0, 3.6, 4.3, 4.9, 5.6, 6.2, 6.9, 7.5, 8.2, 8.8 km s^{-1} . (17+18) 0.9, 1.3, 1.8, 2.2, 2.7 km s^{-1} . (19) 4.6, 5.3, 5.9, 6.6, 7.3, 8.0, 8.7, 9.4, 10.1, 10.7, 11 km s^{-1} . (20) 7.8, 8.8, 9.7, 10.6, 11.6, 12.5, 13.4, 14.4, 15.3 km s^{-1} . (21) 1.6, 2.1, 2.6, 3.2, 3.7, 4.2, 4.7, 5.3 km s^{-1} . (21) 4.7, 5.9, 7.1, 8.4, 9.6, 10.9, 11.1, 13.3, 14.6 km s^{-1} . (23) 0.8, 1.4, 2.0, 2.6, 3.2, 3.8, 4.4, 5.0, 5.6, 6.2, 6.8, 7.4 km s^{-1} . (24) 2.9, 3.4, 3.9, 4.4, 4.9, 5.5, 6.0, 6.5, 7.0 km s^{-1} . (25) 4.1, 4.9, 5.6, 6.3, 7.0, 7.8, 8.5, 9.2, 9.9 km s^{-1} .











3.1.2 The distance of H II regions

CO data are widely used to trace the morphology of molecular clouds. The ¹³CO(1-0) average spectrum in each H II region are presented in Figure 1 (Left panels). From these panels, we can see that spectrum of twenty-two H II regions show multiple velocity components detected along the line of sight, except for H II regions G44.339-0.827, G47.028+0.232, and G49.738-0.616. According to the hydrogen radio recombination line (RRL) velocity components of each H II region given by Anderson et al. (2011), we select the velocity components of ¹³CO(1-0) associated with the H II regions, whose peak is located between two vertical dashed lines in Figure 1 (Left panels). Via Gaussian fits to all the spectra, we obtain the central line velocity (V_{LSR}), the peak intensity (T_{mb}), and full width at half-maximum (FWHM).

Based on the Galactic rotation model of Fich et al. (1989) together with $R_{\odot} = 8.5$ kpc and $V_{\odot} = 220$ km s⁻¹, where V_{\odot} is the circular rotation speed of the Galaxy, we derive the kinematic distances of these H II regions. However, an H II region at a specific radial velocity can be at either the near or far kinematic distance, resulting in a distance ambiguity. The H I self-absorption features product when cool H I clouds absorb the warmer H I emission from the background H II region continuum emission. H I emission/absorption (H I E/A) is considered as an effective method to distinguish the distance ambiguity (Kuchar & Bania 1994, Kolpak et al. 2003, Anderson et al. 2011). Anderson et al. (2011) and

Table 1 H II region sample and CO parameters

Number	Region	l	b	T_{mb}	FWHM	V_{LSR}	$V_{\text{H}\alpha}$	S	D	R	N_{H_2}	n_i	
		deg	deg	(K)	(km s ⁻¹)	(km s ⁻¹)	(km s ⁻¹)	mJy	kpc	pc	cm ⁻²	10 ³ cm ⁻²	
1	G19.504-0.193	19.504	-0.193	2.6	9.4(0.4)	38.9(0.2)	37.8	168	12.8 ^a	2.8	1.5×10 ²²	3.5	N25
2	G19.813+0.010	19.813	+0.010	2.3	4.4(0.2)	57.5(0.1)	60.4	187	11.8 ^b	5.8	6.3×10 ²¹	1.7	N27
3	G23.029-0.405	23.029	-0.405	7.4	7.7(0.2)	74.6(0.1)	76.0	1014	4.7 ^a	3.6	3.6×10 ²²	3.2	
4	G26.824+0.380	26.824	+0.380	2.6	2.4(0.1)	80.9(0.1)	82.0	120	4.9 ^a	2.2	3.9×10 ²¹	1.5	N44
5	G29.007+0.076	29.007	+0.076	2.8	4.8(0.6)	70.3(0.2)	67.7	454	11.5 ^a	7.1	8.4×10 ²¹	1.2	N50
6	G32.587+0.006	32.587	+0.006	2.4	8.4(0.4)	74.5(0.2)	77.4	273	9.7 ^a	4.3	1.3×10 ²²	4.1	N56
7	G32.976-0.334	32.976	-0.334	4.5	4.4(0.1)	49.8(0.1)	49.3	492	11.0 ^a	7.3	1.2×10 ²²	2.5	
8	G33.718-0.410	33.718	-0.410	1.8	3.9(0.2)	49.9(0.1)	53.3	151	3.3 ^a	1.4	4.4×10 ²¹	2.7	
9	G34.325+0.211	34.325	+0.211	3.9	4.0(0.4)	56.9(0.1)	62.9	307	10.3 ^a	5.9	9.8×10 ²¹	1.2	N62
10	G38.353-0.134	38.353	-0.134	1.2	4.0(0.5)	70.3(0.2)	70.5	93.0 ^d	8.6 ^b	3.2	3.0×10 ²¹	0.5	N72
11	G38.643-0.227	38.643	-0.227	2.6	5.1(0.3)	67.9(0.3)	63.8	86	8.7 ^a	3.1	8.3×10 ²¹	2.4	
12	G38.738-0.140	38.738	-0.140	4.1	2.0(0.1)	64.9(0.1)	60.9	213	8.9 ^a	3.2	5.1×10 ²¹	1.1	N73
13	G38.930-0.386	38.930	-0.386	6.6	3.9(0.1)	39.7(0.1)	42.1	38	2.7 ^a	0.7	1.6×10 ²²	6.2	N75
14	G41.132-0.558	41.132	-0.558	2.5	3.8(0.4)	62.4(0.1)	65.5	14.2 ^d	6.4 ^c	2.5	5.9×10 ²¹	1.7	
15	G41.239-0.176	41.239	-0.176	6.1	10.0(0.3)	59.0(0.5)	56.9	440	8.7 ^a	3.8	3.8×10 ²²	9.0	
16	G41.928+0.029	41.928	+0.029	1.6	4.0(0.4)	17.7(0.2)	20.7	620	11.4 ^a	5.7	4.0×10 ²¹	0.8	N80
17	G43.738+0.114	43.738	+0.114	1.8	1.6(0.3)	71.0(0.1)	73.1	15.4 ^d	6.1 ^c	4.2	2.3×10 ²¹	0.6	N89
18	G43.770+0.070	43.770	+0.070	1.2	2.1(0.2)	68.7(0.1)	70.5	360	6.1 ^a	3.8	2.3×10 ²¹	1.2	N90
19	G44.339-0.827	44.339	-0.827	4.0	3.3(0.1)	61.7(0.1)	62.5	136	6.1 ^a	4.1	8.3×10 ²¹	1.7	N92
20	G45.770-0.372	45.770	-0.372	1.8	10.0(0.2)	58.0(0.1)	51.0	15.0 ^d	5.8 ^b	2.2	1.1×10 ²²	0.8	
21	G46.176+0.536	46.176	+0.536	2.1	3.0(0.2)	13.0(0.1)	6.3	30.0 ^d	10.8 ^c	2.5	3.9×10 ²¹	0.9	
22	G47.028+0.232	47.028	+0.232	4.3	3.7(0.1)	56.4(0.1)	56.9	390	5.8 ^a	3.8	1.0×10 ²²	1.6	N98
23	G49.738-0.616	49.738	-0.616	3.0	2.2(0.1)	67.8(0.1)	62.4	37.3 ^d	5.5 ^c	3.8	4.1×10 ²¹	0.8	
24	G50.039-0.274	50.039	-0.274	4.1	2.0(0.2)	62.5(0.1)	60.9	—	5.5 ^c	2.9	5.1×10 ²¹	1.9	N104
25	G50.079+0.571	50.079	+0.571	2.1	3.3(0.1)	-2.0(0.1)	-1.1	195	11.1 ^a	3.8	4.1×10 ²¹	0.5	N105

Notes. ^aDistances are determined with the H I E/A and ¹³CO(1-0) method. ^bDistances are only based on the judgement of ¹³CO(1-0) about the kinematic distance ambiguity. ^cDistances are obtained from the judgement of Bania et al. (2012) about the kinematic distance ambiguity. ^dThe integrated flux at 1.4 GHz.

with this method. Because it is difficult to identify the H I absorption associated with the H II region above error estimates, they did not give the distances of another four H II regions. For H I E/A method, whether every sight line in between the near and far distance existing cool H I clouds is of great importance. The cool H I clouds also are traced by optical thin ¹³CO(1-0), whose emission is relatively stronger. H I E/A, with the addition of ¹³CO(1-0), may accurately resolve the kinematic distance ambiguity. If ¹³CO(1-0) emission coincident with H I absorption is detected between the H II region velocity and the tangent-point velocity, it suggests an H II region at the far distance. On the contrary, it is at near distance. Using H I E/A and ¹³CO(1-0) method, we check the distance of 13 H II regions from GBT H II regions survey, and give the distances of G26.824+0.380, G33.718-0.410, G38.930-0.386, and G41.239+0.029. Because Bania et al. (2012) did not give the H I absorption spectrum of seven H II regions from Arecibo H II regions survey, we yet adopted their judgement about the kinematic distance ambiguity. In addition, we also can not give the judgement of another three H II regions G19.813+0.010, G38.353-0.134, and G45.770-0.372. In

near distance. In Figure 1 (Left panels), we find that if an H II region is far distance, $^{13}\text{CO}(1-0)$ spectrum of the associated molecular clouds has several velocity components in between the tangent-point and system velocity. Because G19.813+0.010 and G38.353-0.134 have several velocity components in between the tangent-point and system velocity, we suggest that both H II regions may be at far distance. The velocity of G45.770-0.372 is near tangent-point velocity, we adopt the tangent-point distance as that of G45.770-0.372. The fitted and obtained results are summarized in Table 1.

3.1.3 The age of H II regions

Above analysis suggest that the characteristics of the surrounding medium may affect the processes of triggered star formation. Moreover, the time scale is also important for deciding the triggered star formation. Assuming each H II region expanding in a homogeneous medium, the dynamical ages of each H II region can be estimated by using the model (Dyson & Williams 1980)

$$t_{\text{HII}} = 7.2 \times 10^4 \left(\frac{R_{\text{HII}}}{\text{pc}} \right)^{4/3} \left(\frac{Q_{\text{Ly}}}{10^{49} \text{s}^{-1}} \right)^{-1/4} \left(\frac{n_i}{10^3 \text{cm}^{-3}} \right)^{-1/2} \text{yr}, \quad (1)$$

where R_{HII} is the radius of the H II region, n_i is the initial number density of the gas and Q_{Ly} is the ionizing luminosity. Because the 8 μm bubble of these H II regions are filled with the 1.4 GHz continuum emission, we take the size of the bubbles as the radius of the H II regions. In previous studies toward several H II regions (Zavagno et al. 2006; Deharveng et al. 2008; Paron et al. 2009, Paron et al. 2011; Pomarès et al. 2009; Dirienzo et al. 2012), they all determined an initial number density of $\sim 10^3 \text{cm}^{-3}$. Here, we also adopt an initial number density of $\sim 10^3 \text{cm}^{-3}$ for all the H II regions. Assuming the emission is optically thin free-free thermal continuum, Q_{Ly} was computed by Mezger et al. (1974)

$$Q_{\text{Ly}} = 4.761 \times 10^{48} a(\nu, T_e)^{-1} \left(\frac{\nu}{\text{GHz}} \right)^{0.1} \left(\frac{T_e}{\text{K}} \right)^{-0.45} \left(\frac{S_\nu}{\text{Jy}} \right) \times \left(\frac{D}{\text{kpc}} \right)^2 \text{photons s}^{-1}, \quad (2)$$

Where ν is the frequency of the observation, S_ν is the observed specific flux density, and D is the distance to the H II region. $a(\nu, T_e)$ is defined by Mezger & Henderson (1967)

$$a(\nu, T_e) = 0.366 \left(\frac{T_e}{\text{K}} \right)^{-0.15} \left(\frac{\nu}{\text{GHz}} \right)^{0.1} \{ \ln[4.995 \times 10^{-2} \times \left(\frac{\nu}{\text{GHz}} \right)^{-1}] + 1.5 \ln \left(\frac{T_e}{\text{K}} \right) \} \quad (3)$$

T_e is the electron temperature given by Paladini et al. (2004) and Tibbs et al. (2012)

$$T_e = (4166 \pm 124) + (314 \pm 20) \times d \text{ K}, \quad (4)$$

According to the rotation curve models of Fich et al. (1989), the Galactocentric distance of H II regions d can be given by

$$d = \frac{V - a_1 V_\odot}{a_2 \omega_\odot}, \quad (5)$$

Where V is the rotation velocity around the Galactic center of an H II region at a Galactocentric distance, and ω_\odot is the rotation velocity and angular velocity of the Sun. The fitting coefficients a_1 , a_2 and ω_\odot are 0.99334, 0.0030385 and 27.5 km s^{-1} (Fich et al. 1989), respectively. In the Arecibo H II region survey, because they did not give the flux density of each H II region at 9 GHz, we replace the flux by that at 1.4 GHz. The obtained electron temperature, ionizing luminosity, and age of 18 H II regions are listed in Table 2. From Table 2, we see that T_e ranges from 5627 K to 6839 K in these H II regions, and the averaged T_e is 6083 K; $a(\nu, T_e)$ is about 0.9 for all the H II regions. Moreover, t_{HII} ranges from $3.0 \times 10^5 \text{ yr}$ to $1.7 \times 10^6 \text{ yr}$,

Table 2 The obtained parameters of H II regions

Number	Region	d (kpc)	T_e K	$a(\nu, T_e)$	Q_{Ly} photons s^{-1}	t_{HII} yr
1	G19.504-0.193	5.6	5935±237	0.9	$(3.7±0.4)×10^{48}$	$(3.6±0.1)×10^5$
2	G19.813+0.010	4.9	5694±221	0.9	$(3.5±0.5)×10^{48}$	$(9.8±0.4)×10^5$
3	G23.029-0.405	4.7	5627±217	0.9	$(3.1±0.4)×10^{48}$	$(5.3±0.2)×10^5$
4	G26.824+0.380	4.8	5673±220	0.9	$(3.9±0.7)×10^{47}$	$(4.7±0.2)×10^5$
5	G29.007+0.076	5.2	5802±228	0.9	$(8.1±0.7)×10^{48}$	$(1.0±0.2)×10^6$
6	G32.587+0.006	5.3	5834±230	0.9	$(3.5±0.3)×10^{48}$	$(6.6±0.1)×10^5$
7	G32.976-0.334	6.1	6079±246	0.9	$(7.9±0.8)×10^{48}$	$(1.1±0.1)×10^6$
8	G33.718-0.410	6.5	6079±246	0.9	$(2.2±0.5)×10^{47}$	$(3.0±0.2)×10^5$
9	G34.325+0.211	5.7	6211±254	0.9	$(4.3±0.5)×10^{48}$	$(9.6±0.3)×10^5$
10	G38.353-0.134	5.8	5958±238	0.9	$(7.6±0.6)×10^{47}$	$(6.5±0.1)×10^5$
11	G38.643-0.227	5.9	5997±241	0.9	$(8.7±0.2)×10^{47}$	$(6.0±0.4)×10^5$
12	G38.738-0.140	6.6	6004±241	0.9	$(2.2±0.2)×10^{48}$	$(4.9±0.1)×10^5$
13	G38.930-0.386	6.0	6240±256	0.9	$(3.6±1.7)×10^{46}$	$(1.1±0.2)×10^6$
14	G41.132-0.558	6.1	6055±244	0.9	$(6.4±1.1)×10^{46}$	$(8.4±0.4)×10^6$
15	G41.239-0.176	7.6	6076±246	0.9	$(4.4±0.9)×10^{48}$	$(5.2±0.2)×10^5$
16	G41.928+0.029	6.3	6551±276	0.9	$(1.0±0.6)×10^{49}$	$(7.3±0.2)×10^5$
17	G43.738+0.114	6.1	6082±246	0.9	$(6.3±1.0)×10^{46}$	$(1.7±0.3)×10^6$
18	G43.770+0.070	6.1	6031±243	0.9	$(1.8±0.3)×10^{48}$	$(6.7±0.3)×10^5$
19	G44.339-0.827	6.1	6090±247	0.9	$(6.7±1.8)×10^{47}$	$(9.3±0.6)×10^5$
20	G45.770-0.372	6.3	6138±250	0.9	$(5.5±0.7)×10^{46}$	$(7.4±0.8)×10^5$
21	G46.176+0.536	7.9	6642±282	0.9	$(3.7±1.1)×10^{47}$	$(5.7±0.2)×10^5$
22	G47.028+0.232	6.3	6155±251	0.9	$(1.7±0.2)×10^{48}$	$(6.6±0.1)×10^5$
23	G49.738-0.616	6.1	6090±247	0.9	$(1.2±1.2)×10^{47}$	$(1.3±0.5)×10^6$
24	G50.039-0.274	6.3	6144±250	0.9	—	—
25	G50.079+0.571	8.5	6839±294	0.9	$(3.0±0.5)×10^{48}$	$(6.4±0.3)×10^5$

3.2 CO molecular gas associated with H II regions

3.2.1 The morphology of the molecular clouds

To show the morphology of the molecular clouds associated with H II regions, we made the velocity-integrated intensity maps of $^{13}\text{CO}(1-0)$ superimposed on each H II region map. The velocity ranges are obtained from the spectrum marked by two vertical dashed lines in Figure 1 (Left panels). In Figure 1 (Right panels), each H II region may coincide with the surrounding molecular clouds. Based on the morphology of molecular clouds associated with H II region, these H II regions will be divided into three groups:

1. Having compact molecular cores are regularly spaced on borders of the H II region traced by PAHs emission, such as G19.504-0.193, G19.813+0.010, G23.029-0.405, G26.824+0.380, G32.587+0.006, G32.976-0.334, G33.718-0.410, G38.643-0.227, G38.738-0.140, G38.930-0.380, G41.928+0.029, G43.738+0.114, G43.770+0.070, G46.176+0.536, and G50.039-0.274. Massive stars form in giant molecular clouds. When UV radiation from these stars products H II regions, they may not far away from their natal molecular clouds. With the expansion of the H II regions, some dense cores may form in a

molecular clouds. Gradually, dense core retain in the compressed layer, while the low density of molecular clouds may be dispersed.

2. Some dense clumps form between H II regions and the surrounding giant molecular clouds, such as G29.007+0.076, G34.325+0.211, G38.353-0.134, G41.132-0.558, G41.239-0.176, G44.339-0.827, G45.770-0.372, G47.028+0.232, and G49.738-0.616. When massive stars form on or near borders of giant molecular clouds, the expansion of H II regions accumulate the molecular gas between the giant molecular clouds and H II region. Hence, some dense clumps form in the compressed layer.

3. Molecular clouds cover the whole H II regions, such as G50.079+0.571. It indicates that these H II regions are still embedded in the giant molecular clouds.

In H II regions G29.007+0.076, G44.339-0.827, and G47.028+0.232, the PAHs emission all show a cometary structure. Moreover, the whole filamentary molecular cloud interacted with PAHs emission of G47.028+0.232 exhibits a cometary structure. The three H II regions support the RDI model. The rest of the H II regions in the groups 1 and 2, the molecular clouds with compact core regularly distribute around the PAHs emission, it is strong evidence in favor of the CC model. In addition, with the evolution of H II region, the H II regions in group 3 may become the morphology of that in groups 1 and 2.

3.2.2 The physical parameters of the molecular clouds

Assuming local thermodynamical equilibrium (LTE) and using the $^{13}\text{CO}(1-0)$ line, the column density of the clumps in cm^{-2} was estimated to be Garden et al. (1991)

$$N_{\text{H}_2} = 1.25 \times 10^{15} \int T_{\text{mb}} dv \text{ cm}^{-2}, \quad (6)$$

where dv is the velocity range in km s^{-1} . Here we adopt a relation $N_{\text{H}_2} \approx 5 \times 10^5 N_{^{13}\text{CO}}$ (Simon et al. 2001) and the average excitation temperature of 20 K from previous studies (Paron et al. 2011, Dirienzo et al. 2012). If the clumps are approximately spherical in shape, the mean number density H_2 is $n(i)=1.62 \times 10^{-19} N_{\text{H}_2}/L$, where L is the clump diameter in parsecs (pc). The clump may be irregularly shaped, we use an effective radius, which is the radius of a circle that has the same solid angle on the sky as the clump. The derived column density of each clump is listed in Table 1, which range from $2.3 \times 10^{21} \text{ cm}^{-2}$ to $7.3 \times 10^{22} \text{ cm}^{-2}$. These values are compatible with the theoretical predictions of Whitworth et al. 1994, who show that for a wide range of input parameters, the gravitational fragmentation of a shocked layer occurs when the column density of this layer reaches a value $\sim 6.0 \times 10^{21} \text{ cm}^{-2}$. In 25 H II regions, the derived column density of 21 H II regions are lower than value of Whitworth et al. 1994, implying that the shocked layer of these H II regions have been gravitationally fragmented.

3.2.3 Outflow detected

Millimeter-wavelength continuum surveys of the Galactic plane provide the most efficient way to find molecular clumps that are the likely formation sites of massive stars and star clusters. According to the Bolocam Galactic Plane Survey (BGPS), we selected the BGPS sources in the surrounding of each H II region. From Figure 1 (Right), we can see that there are several BGPS sources (green plus) distributed along the bubble of each H II region, except for G41.132-0.558, G41.928+0.029, G43.738, G43.770,

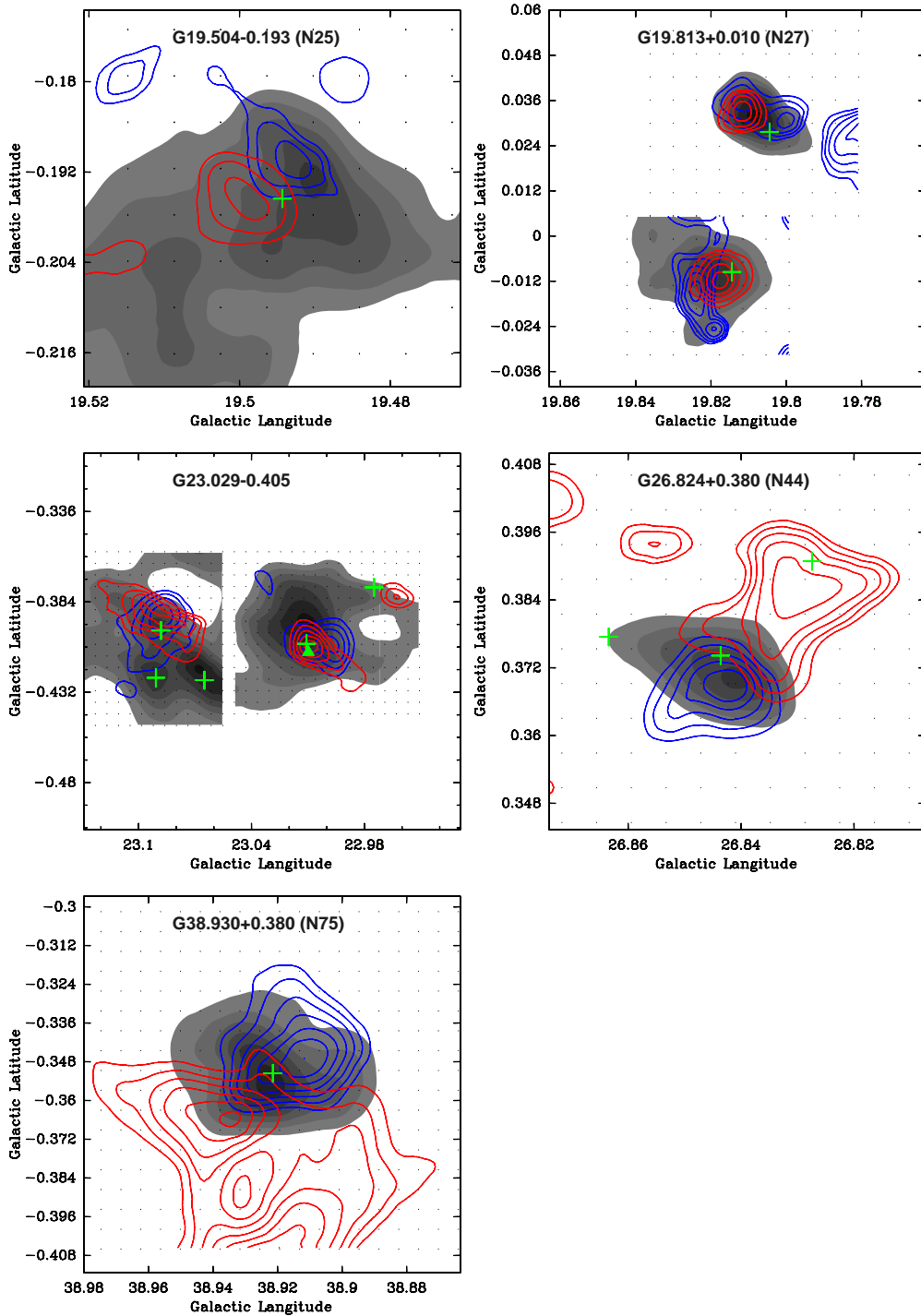


Fig. 2 The contour maps of Outflow overlaid with the $^{13}\text{CO}(1-0)$ emission of each clump (gray scale). G19.504-0.193: The blue contour levels are 0.9, 1.0, 1.1 km s^{-1} , while the red contour levels are 0.9, 1.0, 1.1 km s^{-1} . G19.813+0.01: (Top) The blue contour levels are 0.5, 0.6, 0.7, 0.8 km s^{-1} , while the red contour levels are 0.5, 0.6, 0.7, 0.8 km s^{-1} . (Bottom) The blue contour levels are 0.2, 0.3, 0.4, 0.5, 0.6 km s^{-1} , while the red contour levels are 0.9, 1.1, 1.2, 1.3, 1.4 km s^{-1} . G23.029-0.405: (Left) The blue contour levels are 10.0, 10.7, 7.0, 8.0, 9.0, 10.0 km s^{-1} , while the red contour levels are 5.0, 6.0, 7.0, 8.0 km s^{-1} . (Right) The blue contour levels are 10.0, 10.7, 11.4, 12.1, 12.8, 13.6, 14.3 km s^{-1} , while the red contour levels are 10.0, 10.7, 11.4, 12.1, 12.8, 13.6, 14.3 km s^{-1} . G26.824+0.380: The blue contour levels are 0.5, 0.6, 0.7, 0.8, 0.9

Table 3 The obtained parameters of outflow

Number	Region	BGPS	l deg	d deg	t_{out} yr
1	G19.504-0.193	G19.490-0.197	19.494	-0.196	2.7×10^5
2	G19.813+0.010	G19.818-0.009	19.814	-0.010	6.5×10^5
		G19.806+0.033	19.804	0.028	6.4×10^5
3	G23.029-0.405	G23.012-0.410	23.011	-0.406	2.0×10^5
		G23.090-0.394	23.088	-0.399	2.5×10^5
4	G26.824+0.380	G26.843+0.375	26.844	0.374	3.8×10^5
5	G38.930+0.380	G38.920-0.352	38.921	-0.352	5.1×10^5

BGPS sources are located at the center of molecular cores. An outflow is strong evidence of the earlier star-forming activity. In order to search for the activity of star-forming activity, we detect outflows for these BGPS sources associated with H II regions and molecular cores. If several cores are linked together, then it is difficult to determine the component of the outflows. Hence, we only selected the BGPS sources associated with the isolated cores. In 25 H II regions, we find that the molecular cores associated with 7 H II regions satisfy the above criterion. For these molecular cores, we first drew position-velocity (P-V) diagrams. According to the P-V diagrams, we selected the integrated range of wings and determined the outflow intensities of red and blue lobes. Seven molecular outflows were identified by the contours of integrated intensities of $^{13}\text{CO}(1-0)$ line wings in H II regions G19.504-0.193, G19.813+0.01, G23.029-0.405, G26.824+0.380 and G38.930+0.380. For the H II region G38.930+0.380, we have performed a detailed analysis with $^{12}\text{CO } J=1-0$, $^{13}\text{CO } J=1-0$ and $\text{C}^{18}\text{O } J=1-0$ lines (Xu et al. 2013). The dynamic timescale of each outflow is estimated by equation $t_{\text{out}}=9.78 \times 10^5 R/V$ (yr), where V in km s^{-1} is the maximum flow velocity relative to the cloud systemic velocity, and R in pc is the outflow size defined by the length of the begin-to-end flow extension for each blueshifted and redshifted lobes. The mean dynamic timescale of each outflow is listed in Table 3.

4 DISCUSSION

4.1 Assessment of triggered star formation

IRAS Point Source Catalog has reveal a number of stellar objects, which are younger than pre-main sequence stars (Beichman et al. 1986, Fukui et al. 1989). Hence, the *IRAS* point source is a good signpost of very early stages of star formation. In order to explore a causal relationship between the H II regions and star formation, we have searched for protostellar candidates in the *IRAS* Point Source Catalog that fulfill the following selection criteria (Jankes et al. 1992 & Xu et al. 2011): (1) $F_{100} \geq 20$ Jy, (2) $1.2 \leq F_{100}/F_{60} \leq 6.0$, (3) $F_{25} \leq F_{60}$, and (4) $R_{IRAS} \leq 1.5 \cdot R_{\text{HII}}$, where F_{25} , F_{60} and F_{100} are the infrared fluxes at three IR bands ($25\mu\text{m}$, $60\mu\text{m}$ and $100\mu\text{m}$), respectively. The first criterion selects only strong sources. The second and third discriminate against cold IR Point sources probably associated with cool stars, planetary nebulae, and cirrus clumps. While the fourth guarantees that the search diameter (R_{IRAS}) include the complete surface of H II regions. *IRAS* sources were found in a search circle within

above criteria. The name, coordinates, and flux at the 12, 25, 60, 100 μm of these *IRAS* point sources are listed in Table 3. Infrared luminosity (Casoli et al. 1986) and dust temperature (Henning et al. 1990) are expressed respectively as,

$$L_{\text{IR}} = (20.653 \times F_{12} + 7.538 \times F_{25} + 4.578 \times F_{60} + 1.762 \times F_{100}) \times D^2 \times 0.30, \quad (7)$$

$$T_{\text{d}} = \frac{96}{(3 + \beta) \ln(100/60) - \ln(F_{60}/F_{100})}, \quad (8)$$

Where D is the distance from the sun in kpc. The emissivity index of dust particle (β) is assumed to be 2. The calculated results are presented in Table 3. From the Table 3, we can see that the infrared luminosity L_{IR} of each *IRAS* source is larger than $10^3 L_{\odot}$, which is associated with that of bubble N131 (Zhang et al. 2013). The *IRAS* sources associated with the BRCs have L_{IR} from ~ 10 to $10^3 L_{\odot}$ (Sugitani et al. 1991). In addition, Junkes et al. 1992 found 17 *IRAS* sources associated with SNR G54.4-0.3, 16 of these sources L_{IR} are $\leq 10^3 L_{\odot}$. Similarly, the luminosity L_{IR} of all the *IRAS* sources surrounding SNR IC443 are $< 10^3 L_{\odot}$ (Xu et al. 2011). BRCs found in H II regions are potential sites of triggered star formation by RDI process. We suggest that the process of star formation triggered by SNRs may be similar to RDI. Figure 1 (Right panels) also shows that the spatial distribution of the selected *IRAS* sources in 17 H II regions. From Figure 1 (Right panels), we see that all the *IRAS* sources are associated with PAH emission and some *IRAS* sources are located at the peak of ^{13}CO molecular clumps, indicating that these *IRAS* sources with the larger infrared luminosity may be triggered by CC process.

To further search for primary tracers of the star-formation activity in the surroundings of H II regions, we used the GLIMPSE I catalog, which consists of point sources that are detected at least twice in one band. Based on the photometric criteria of Allen et al. (2004), we search for young star objects (YSO) candidates within a circle of > 1.5 radius centered at each H II regions. From the database, we constructed a $[5.8] - [8.0]$ versus $[3.6] - [4.5]$ color-color (CC) diagram for each H II region to identify Class I and Class II YSOs. Class I sources (10^5 yr) are protostars with circumstellar envelopes, Class II sources (10^6 yr) are disk-dominated objects. Figure 1 (Right panels) shows the spatial distribution of both Class I and Class II sources. From Figures 1 (Right panels), we note that some Class I sources are asymmetrically distributed only in H II region G29.007+0.076, G44.339-0.827, and G47.028+0.232, and are mostly concentrated on the interacting regions between these H II regions and the surrounding molecular clouds. In H II regions G29.007+0.076 and G47.028+0.232, the Class I sources in the interacting regions are closed to the center of the H II regions compared to the Class II sources. The existence of Class I and Class II sources may also indicate star formation activity.

Comparing the age of each H II region with the characteristic star-formation timescales, we conclude that the three H II regions can trigger the clustered star formation. In addition, we find that the PAHs emission of the three H II regions is stronger closed to the molecular clouds, and all show the cometary globule, suggesting these Class I and Class II sources may be triggered by RDI process. In addition, we for the first time detected seven molecular outflows in H II regions G19.504-0.193, G19.813+0.01, G23.029-0.405, G26.824+0.380 and G38.930+0.380. The mean dynamic timescale of each outflow is larger than the age of the corresponding H II regions. Hence, we conclude that these outflow sources may be triggered by the corresponding H II regions, but the observations at higher spatial resolution are needed to resolve the

Table 4 Selected IR point sources near 25 H II regions: IR flux densities, dust temperatures and IR luminosities.

Number	Source	l deg	b deg	F_{12} [Jy]	F_{25} [Jy]	F_{60} [Jy]	F_{100} [Jy]	T_d [K]	L_{IR} [$\times 10^4 L_\odot$]
1	IRAS 18244-1201	19.524	-0.185	5.06	33.3	732.7	2011.0	26.9	35.7
2	-	-	-	-	-	-	-	-	-
3	IRAS 18317-0903	22.987	-0.381	4.8	45.1	1144.0	4999.0	23.8	9.6
	IRAS 18319-0903	23.012	-0.422	4.8	25.0	1144.0	4592.0	24.3	9.1
4	-	-	-	-	-	-	-	-	-
5	IRAS 18413-0331	28.995	0.082	4.8	14.3	335.1	577.5	31.0	11.0
6	IRAS 18482-0021	32.590	0.001	10.0	8.2	109.7	470.8	23.9	4.5
7	IRAS 18501-0009	32.998	-0.338	3.0	10.4	162.1	737.1	23.5	7.9
8	IRAS 18518+0026	33.716	-0.420	3.1	1.0	39.8	224.7	22.4	0.2
9	IRAS 18507+0118	34.362	0.206	2.5	12.1	765.4	1948.0	27.5	22.5
10	-	-	-	-	-	-	-	-	-
11	IRAS 19002+0454	38.645	-0.225	2.2	11.3	120.3	285.6	28.1	2.7
12	-	-	-	-	-	-	-	-	-
13	IRAS 19015+0503	38.933	-0.456	2.2	6.8	497.2	1156.0	28.2	14.6
14	IRAS 19060+0657	41.136	-0.553	3.2	2.8	55.1	141.8	27.4	0.7
15	-	-	-	-	-	-	-	-	-
16	IRAS 19054+0754	41.916	0.007	1.6	1.5	16.8	51.0	26.2	0.8
	IRAS 19054+0755	41.923	0.035	0.6	4.1	84.4	186.7	28.7	3.0
17	IRAS 19086+0935	43.762	0.108	2.1	1.5	73.8	356.7	2.3	1.1
18	IRAS 19088+0935	43.788	0.059	3.1	17.1	71.0	235.1	25.6	1.1
19	IRAS 19130+0940	44.356	-0.822	3.5	0.9	150.9	557.2	24.9	2.0
20	-	-	-	-	-	-	-	-	-
21	IRAS 19116+1156	46.195	0.539	7.1	6.6	110.2	391.7	25.1	4.9
	IRAS 19116+1157	46.213	0.548	3.9	3.2	388.3	1297.0	25.5	14.6
	IRAS 19116+1155	46.182	0.531	2.5	5.2	486.2	1454.0	26.3	17.1
22	IRAS 19143+1232	47.029	0.241	3.0	6.9	169.2	519.4	26.1	1.8
23	IRAS 19227+1431	49.746	-0.623	3.1	2.2	24.8	75.7	26.2	0.3
24	-	-	-	-	-	-	-	-	-
25	IRAS 19191+1522	50.075	-0.560	2.5	7.6	206.4	607.1	26.4	7.8

5 CONCLUSIONS

In this work, we have performed a detailed analysis of the environment of 25 H II regions with bubble morphologies in $^{13}\text{CO}(1-0)$ and infrared data. These H II regions at $8 \mu\text{m}$ show the morphology of the complete and partial bubble, indicating PAHs emission is destroyed inside the ionized region. Each H II region may be associated with the surrounding molecular clouds. In 25 H II regions, the derived column density of 21 H II regions are larger than value of Whitworth et al. (1994), implying that the shocked layer of these H II regions have been gravitationally fragmented. We derived that the electron temperature ranges from 5627 K to 6839 K in these H II regions, and the averaged electron temperature is 6083 K. Moreover, the age of all the H II regions is from 3.0×10^5 yr to 1.7×10^6 yr, and the mean age is 7.7×10^5 yr. We selected 23 young *IRAS* sources with the larger infrared luminosity ($> 10^3 L_\odot$) in 19 H II regions, which

are concentrated around H II regions G29.007+0.076, G44.339-0.827, and G47.028+0.232, which appear to be sites of ongoing star formation. The PAHs emission of the three H II regions all show the cometary globule. Comparing the age of each H II region and the characteristic timescales for star formation, we conclude that the three H II region can trigger the clustered star formation by RDI process. In addition, we for the first time detected seven molecular outflows in the five H II regions. These outflow sources may be related to the corresponding H II regions.

Acknowledgements We thank an anonymous referee for very useful suggestions

References

- Allen, L. E., Calvet, N., D'Alessio, P., 2004, *ApJS*, 154, 363
- Anderson, L. D., Bania, T. M., Balser, D. S., & Rood, R. T. 2011, *ApJ*, 194, 32
- Anderson, L. D., Bania, T. M., Balser, D. S., & Rood, R. T. 2011, *ApJ*, 194, 32
- Bania, T. M., Anderson, L. D., Balser, Dana S., & Rood, R. T. 2010, *ApJ*, 718, L106
- Bania, T. M., Anderson, L. D., Balser, D. S. 2012, *ApJ*, 759, 96
- Beichman, C. A., Myers, P. C., Emerson, J. P., Harris, S., Mathieu, R., Benson, P. J., & Jennings, R. E. 1986, *ApJ*, 307, 337
- Casoli, F., Combes, F., Dupraz, C., Gerin, M., & Boulanger, F., 1986, *A&A*, 169, 281
- Churchwell, E., Povich, M. S., Allen, D., et al. 2006, *ApJ*, 649, 759
- Condon, J. J., Cotton, W. D, Greisen, E. W., et al., 1998, *AJ*, 115, 1693
- Dale, J. E., Bonnell, I. A., & Whitworth, A. P. 2007, *MNRAS*, 375, 1291
- Deharveng, L., Lefloch, B., Kurtz, S., et al. 2008, *A&A*, 482, 585
- Dewangan, L. K., Ojha, D. K., Anandarao, B. J., et al. 2012, *ApJ*, 756, 151
- Dirienzo, W. J., Indebetouw, R., Brogan, C. 2012, *ApJ*, 144, 173
- Dyson, J. E., & Williams, D. A. 1980, *Physics of the interstellar medium*, ed. Dyson, J. E. & Williams, D. A.
- Fazio, G. G., Hora, J. L., Allen, L. E., et al. 2004, *ApJS*, 154, 10
- Fich, M., Blitz, L., & Stark, A. A., 1989, *ApJ*, 342, 272
- Fich, M., Blitz, L., & Stark, A. A., 1989, *ApJ*, 342, 272
- Fukui, Y., Sugitani, K., Takaba, H. 1989, *Nature*, 342, 171
- Garden, R. P., Hayashi, M., Hasegawa, T., et al., 1991, *ApJ*, 374, 540
- Henning, Th., Pfau, W., & Altenhoff, W. J., 1990, *A&A*, 227, 542
- Jackson, J. M., Rathborne, J. M., Shah, R. Y. et al. 2006, *ApJS*, 163, 145
- Junkes, N., Furst, E., Reich, W. 1992, *A&A*, 261, 289
- Kolpak, M. A., Jackson, J. M., Bania, T. M., Clemens, D. P., & Dickey, J. M. 2003, *ApJ*, 582, 756
- Kuchar, N., & Bania, T. W. 1994, *ApJ*, 436, 117
- Mezger, P. G., & Henderson, A. P. 1967, *ApJ*, 147, 471
- Mezger, P. G., Smith, L. F., & Churchwell, E. 1974, *A&A*, 32, 269
- Paron, S., Ortega, M. E., Rubio, M. 2009, *A&A*, 498, 445
- Paron, S., Petriella, A., & Ortega, M. E. 2011, *A&A*, 525, 9
- Paladini, R., Davies, R. D., & De Zotti, G. 2004, *MNRAS*, 347, 237
- Pomarès, M., Zavagno, A., Deharveng, L., et al. 2009, *A&A*, 494, 987
- Reipurth, B. 1983, *A&A*, 117, 183
- Sandford, II, M. T., Whitaker, R. W., & Klein, R. I. 1982, *ApJ*, 260, 183
- Simon, R., Jackson, J. M., Clemens, D. P., Bania, T. M., & Heyer, M. H. 2001, *ApJ*, 551, 747
- Sugitani, K., Fukui, Y., & Ogura, K. 1991, *ApJ*, 77, 59
- Su, Y., Chen, Y., & Yang, J. 2009, *ApJ*, 694, 376
- Tibbs, C. T., Paladini, R., Compiègne, M., et al. 2012, *ApJ*, 754, 94
- Whitworth, A., Bhattal, A., Chapman, S., Disney, M., & Turner, J. 1994, *MNRAS*, 268, 291
- Xu, J.-L., Wang, J.-J., & Martin, M. 2011, *ApJ*, 727, 81
- Xu, J.-L., & Wang, J.-J. 2012, *A&A*, 543, 24.

- Zavagno, A., Deharveng, L., Comerón, F., et al. 2006, *A&A*, 446, 171
- Zavagno, A., Russeil, D., Motte, F., et al. 2010, *A&A*, 518, 101
- Zhang, C.-P., Wang, J.-J., Xu, J.-L. 2013, *A&A*, 550, 117
- Zhou, X., Chen, Y., Su, Y., & Yang, J. 2009, *ApJ*, 691, 516
- Zinnecker, H., & Yorke, H. W. 2007, *ARA&A*, 45, 481